Rejuvenating IRS: AoI-based Low Overhead Reconfiguration Design

Jorge Torres Gómez*, Joana Angjo*, Moritz Garkisch†, Vahid Jamali‡, Robert Schober†, and Falko Dressler*
*School of Electrical Engineering and Computer Science, TU Berlin, Berlin, Germany
†Institute for Digital Communications, University of Erlangen-Nuremberg, Erlangen, Germany
‡Department of Electrical Engineering and Information Technology, Technical University of Darmstadt, Germany

***Abstract*—Intelligent reflective surface (IRS) technologies help mitigate undesirable effects in wireless links by steering the communication signal between transmitters and receivers. IRS elements are configured to adjust the phase of the reflected signal for a user's location and enhance the perceived signal-to-noise ratio (SNR). In this way, an IRS improves the communication link but inevitably introduces more communication overhead. This occurs especially in mobile scenarios, where the user's position must be frequently estimated to re-adjust the IRS elements periodically. Such an operation requires balancing the amount of training versus the data time slots to optimize the communication performance in the link. Aiming to study this balance with the age of information (AoI) framework, we address the question of how often an IRS needs to be updated with the lowest possible overhead and the maximum of freshness of information. We derive the corresponding analytical solution for a mobile scenario, where the transmitter is static and the mobile user (MU) follows a random waypoint mobility model. We provide a closed-form expression for the average peak age of information (PAoI), as a metric to evaluate the impact of the IRS update frequency. As for the performance evaluation, we consider a realistic scenario following the IEEE 802.11ad standard, targeting the mmWave band. Our results reveal that the minimum achievable average PAoI is in the microsecond range and the optimal IRS update period is in the seconds range, causing 9 % overhead in the link when the MU moves at a velocity of 1 m/s.**

***Index Terms*—Age of information, intelligent reflecting surfaces, mobility, mmWave, WiFi.**

I. Introduction

REALIZING intelligent reflective surface (IRS)-assisted communication links are considered a powerful paradigm to enhance next-generation wireless communication. IRSs allow reshaping the communication channel for improved quality of service (QoS) through low-cost reflective patches organized as planar arrays [1]. This technology enables the steering of communication signals by adjusting the phase introduced by the IRS elements, enhancing signal-to-noise ratio (SNR) levels in targeted regions. Such a solution finds application in mmWave band networks, at scalable cost and power consumption levels [2].

A key aspect of ensuring a given SNR is the use of low-complexity methods to reconfigure the IRS elements. Examples include the partitioning of the IRS array into multiple tiles [3], the development of joint beam training and positioning for fast beam-tracking schemes [4], and the use of variable-size codebooks [5]. Besides, for the communication system to operate, the passive IRS elements must be frequently updated using these methods while keeping track of the mobile users (MUs) position in the network [6]. Consequently, the IRS should track the MU position regularly and reconfigure the IRS elements to illuminate the MU with the new position.

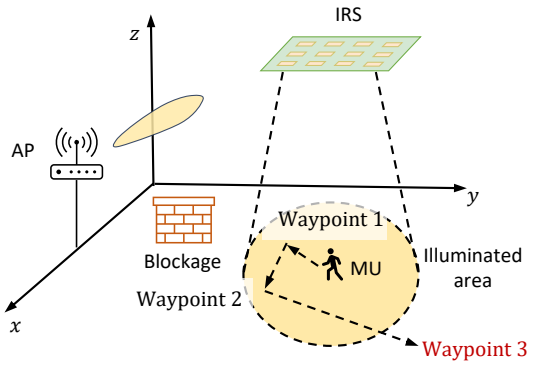

Fig. 1: Illustration of the mobility of the mobile user (MU) and IRS coverage area.

We illustrate this requirement with the diagram depicted in Fig. 1, where an MU is connected to an access point (AP) whenever it is located within the illuminated area, as there is non-line-of-sight (NLOS) link to the AP. As a result, the quality of the communication link in this mobile scenario is determined not only by the SNR in the link but also by the overhead incurred each time the MU is localized and the IRS is updated, as during these time slots, data transmissions are interrupted. The more frequently the IRS is updated, the better the guarantees for the SNR, but the fewer the opportunities for the users to transmit data, i.e., increased overhead. On the contrary, the less frequently the IRS is updated, the lower the communication link quality as the MU might leave the illuminated area and experience a drop in SNR.

In this scenario, a training protocol for the IRS reconfiguration can be designed that accounts for the update period with the mobility of the MUs [7]. Reported examples in the literature evaluate the update period assuming the worst-case scenario, where a fixed channel coherence time is considered, as in [8], or by assuming the MU deterministically moves to the edge of the coverage area and at a constant speed [9]. More straightforwardly, the authors in [10] evaluate the IRS reconfiguration period to maximize the link's sum rate. The pilot interval to estimate the channel is increased (reducing overhead) until the impact of channel variability starts

decrementing the SNR. While this study explicitly assesses the time configuration period, it examines the effect of MU mobility solely through its velocity component, overlooking its specific mobility pattern.

In this paper, we adopt a more holistic approach utilizing the age of information (AoI) concept to evaluate the IRS update period. The AoI concept encompasses all aspects of the communication link in a single formulation, including packet transmission periods, channel impairments, and delays within the communication pipeline [11], [12]. AoI-based solutions for IRS-assisted links have been previously reported to maximize information freshness. Existing research targets packet scheduling mechanisms in various network settings, e.g., in IRS-empowered unmanned aerial vehicle (UAV) systems [13], [14], wireless information and power transfer (SWIPT) [15], non-orthogonal multiple access (NOMA) networks [16], and IRS-assisted secure communications [17]. Nonetheless, these studies neglect the immediate effects of overhead from reconfiguration packets, particularly when balancing overhead and communication performance in mobile contexts.

We apply the AoI in the mobile scenario depicted in Fig. 7, where a MU does not have line-of-sight (LOS) condition to an AP and communication occurs through the IRS only. We research a reconfiguration strategy for a low-overhead transmission scheme focusing on minimizing the peak age of information (PAoI) metric. We identify this approach as the missing component in today's literature for evaluating the optimal update period of the IRS elements. Pursuing this research direction, our main contributions can be summarized as follows:

- We characterize the dynamic behavior of an IRS-assisted link as a Markov regenerative process (MRGP), explicitly accounting for MU mobility and the underlying transmission scheme.
- We formulate the trade-off between performance and overhead in an AoI-based framework. The proposed AoI framework encompasses the dynamics of the IRS-assisted link and can be used to determine the optimal periodicity for updating the IRS.[1]
- We propose a three-step methodology to exploit this theoretical model in a practical communication scenario. We examine the overhead for realistic WiFi communication links in the mmWave band, however, this methodology also applies to other communication scenarios.

The rest of this paper is organized as follows. We discuss the reported research on the join topics IRS and AoI in Section II. We sketch the system model in Section III detailing the transmission setup. We model the link status model as a semi-Markov regeneration process in Section IV. The AoI-based problem formulation is presented in Section V, deriving analytical expressions to evaluate the minimum of the average PAoI metric. We assess the performance in Section VI using the derived analytical expressions. In this section, we also illustrate the impact of overhead and mobility on the average PAoI metric for a realistic WiFi link.[2] Finally, we provide concluding remarks in Section VII.

[1]This framework establishes the basis for the formulation and solution of optimization problems for the communication system design in future work.

II. Related Work

AoI has been used in IRS-assisted networks to characterize the freshness of monitored sensor data. Existing studies target various scenarios like Internet of Things (IoT) networks in urban environments [18], where power and latencies are predominant restrictions, and also UAV-assisted scenarios [12], [14], [19]. Furthermore, AoI has also been used to maximize the freshness of data between two users in covert communication links as in [17], [20].

The considered systems comprise links between nodes and base stations (BSs) or APs in urban environments with one [16], [17], [20], [21] or multiple IRSs [18]. More complex scenarios also include energy transfer from APs to nodes using simultaneous transmitting and reflecting IRSs [22], as well as SWIPT mechanisms [15], [23]. Other reports consider communication between UAVs and IoT nodes through a fixed IRS [14]. Furthermore, towards enhancing flexibility during deployment, existing solutions have integrated IRSs with UAV to avoid the latency introduced by relay nodes at the UAV [12], [19], [24].

The freshness of data is mostly optimized using the average AoI metric (and less frequently using the average PAoI as, e.g., in [16]). The AoI metric is used, e.g., in combination with communication schemes like hybrid automatic repeat request (HARQ) error-control protocols [18], channel access mechanisms with NOMA [19], [22], and full-duplex communication links [21]. Integrating UAV-assisted links, the information freshness is evaluated readily with the average AoI metric [12], using the average of AoI increase [14], and also as a multi-objective function using an ultra-reliable low-latency communication (URLLC)-based formulation, as in [24].

AoI-based solutions often come with certain restrictions. The power level is typically part of the restriction due to the limited battery capabilities of IoT nodes. Reported research combines the communication reliability with the outage probability [18], or the communication covertness limiting the detection probabilities of unauthorized users [17], [20]. Further constraints include successful packet reception levels [16], SNR thresholds, the scheduling of the number of nodes per time slot, and the mobility range of UAVs [12]–[15], [19], [24].

Solutions using the AoI formulation are developed both numerically and via machine learning (ML)-based methods, aiming to control communication and mobility parameters jointly. For instance, the alternating optimization algorithm in [23] is used to find the beamforming vectors, configure the IRS, and the scheduling of nodes. Genetic algorithms are also reported to optimize the power and time scheduling of nodes [22]. Successive convex approximation (SCA) [12], [17] and the block coordinate descent (BCD) algorithms [19] are reported to jointly control UAV mobility and the scheduling

[2]We provide open access to the code that evaluates the AoI metrics in IRS-assisted link in https://github.com/tkn-tub/IRS_Rejuvenation

of IoT nodes [19], as well as to jointly configure the IRS and the packet length [17]. Using deep reinforcement learning (DRL), off-on policies have been reported for various joint designs with reinforcement Q-learning, deep Q-network (DQN), and proximal policy optimization (PPO) policies. For instance, reinforcement Q-learning is reported to jointly find the location of the UAV-IRS [24]. IRS and the packet service time are also jointly configured with DQN [14]. DQNs has also been proposed for the evaluation of the transmission scheduling only, as in [24].

Despite the rich literature and the optimal configuration of IRSs, there is no solution for the optimal periodicity for reconfiguring the IRS elements. Analyzing the optimal periodicity allows determining the right balance between the overhead introduced for configuring the IRS and the communication performance. As we continue in the following sections, we will illustrate the relevancy of this concern in mobile scenarios, where the IRS has to be frequently updated to guarantee a good communication performance, i.e., a particular QoS level.

III. System Model

We study a communication downlink between an AP and an MU that moves at walking speed. The communication link is facilitated via the reflection of an IRS, where we assume NLOS conditions between the AP and the MU, as depicted in Fig. 1. The IRS provides coverage for a circular area of radius r_{in}, a shape that has also been considered in wireless scenarios, as in [25].[3] The achieved SNR is sufficiently high in the illuminated area to realize error-free transmissions with a certain data rate. Under this general model, three important elements of the communication link include: i) the IRS-assisted link abstracted with the SNR in the illuminated area, ii) the transmission frame in the downlink delimiting the time slots for communication, and iii) the communication-link dynamics given the MU mobility model. We elaborate on these elements in the following subsections.

A. IRS-assisted Link Model

We model the impact of the IRS-assisted link using the SNR in the MU plane. At a given observation point in the xy plane, denoted as $\mathbf{p}_{\text{obs}}$, the SNR is given by the relation

$$\text{SNR}(\mathbf{p}_{\text{obs}}) = |g_{\text{IRS}}(\mathbf{p}_{\text{obs}})|^2 \frac{P_{\text{Tx}} \text{PL}_{\text{AP,IRS}} \text{PL}_{\text{IRS},\mathbf{p}_{\text{obs}}}}{P_{\text{N}}}, \quad (1)$$

which follows from [3, Eq. (2)], where P_{Tx} is the transmit power, P_{N} is the noise power, the variable $\text{PL}_{\text{AP,IRS}}$ is the free-space pathloss AP-to-IRS link, given by

$$\text{PL}_{\text{AP,IRS}} = \left(\frac{\lambda}{2\pi ||\mathbf{p}_{\text{IRS}} - \mathbf{p}_{\text{AP}}||} \right)^2, \quad (2)$$

where $\lambda = c/f$ is the wavelength of the transmitted signal, c is the speed of light, and f the center frequency for transmission. Besides, $\mathbf{p}_{\text{IRS}}$ denotes the position of the IRS, $\mathbf{p}_{\text{AP}}$ refers to the position of the AP, and $||\cdot||$ is the norm of a vector.

In Eq. (1), $\text{PL}_{\text{IRS},\mathbf{p}_{\text{obs}}}$ is the free-space pathloss between the IRS and the observation point $\mathbf{p}_{\text{obs}}$ (within the MU mobility plane), given by

$$\text{PL}_{\text{IRS},\mathbf{p}_{\text{obs}}} = \left(\frac{\lambda}{2\pi ||\mathbf{p}_{\text{obs}} - \mathbf{p}_{\text{IRS}}||} \right)^2. \quad (3)$$

Furthermore, $g_{\text{IRS}}(\mathbf{p}_{\text{obs}})$ is the IRS gain, evaluated as the sum of gains for each individual IRS-element, given by

$$g_{\text{IRS}}(\mathbf{p}_{\text{obs}}) = \tilde{g} \sum_{n=1}^{N} \mathbb{I}_{\{||\mathbf{p}_n - \mathbf{p}_{\text{IRS}}|| < \frac{L}{2}\}} \times \quad (4)$$
$$\times e^{j\frac{2\pi}{\lambda}(||\mathbf{p}_{\text{n}} - \mathbf{p}_{\text{AP}}|| + ||\mathbf{p}_{\text{obs}} - \mathbf{p}_n||)} e^{j\omega_{\text{IRS}}(n)},$$

which follows from [26, Eq. (4)], where N is the total number of IRS elements, L is the radius of the circumference inscribed in the IRS plane (the purpose of this parameter is elaborated later in this section), $\omega_{\text{IRS}}(n)$ is the IRS phase shift corresponding to its n-th element, $\mathbf{p}_{\text{n}}$ is the position of the n-th IRS element, and $\tilde{g}$ denotes the maximum gain of a given IRS element, evaluated as

$$\tilde{g} = \frac{\sqrt{4\pi} d_w d_h}{\lambda}; \quad (5)$$

see [3, Eq. (12)], where d_w and d_h refer to the width and the height of the unit cell, respectively.

In Eq. (1), the IRS phase shift coefficients are the primary design variables, while the remaining parameters are predetermined by the scenario setup, as illustrated in Fig. 1. The value of $\omega_{\text{IRS}}(n)$ is obtained based on the design proposed in [27, Sec. III. B 2)] and [26, Sec. III A] to illuminate with a given SNR the widest area possible. This coefficients design realizes a linear mapping function; see [27, Eqs. (6) and (7)], which focuses each radiation point from the IRS into an arbitrary rectangular area in the xy plane. The size of the projected rectangular area is adjusted with the beam-width parameters Δx and Δy in [26, Eq. (6)] and [27, Eq. (7)]. However, to generate a circular illuminated area, we programmatically disconnect those IRS elements that are not contributing to the circular shape; that is, the corresponding coefficients are set to zero in (4) with the indicator function $\mathbb{I}$. The indicator function is equal to 1, whenever the position of the IRS element is within the inscribed circle of the IRS, as follows from the condition $(||\mathbf{p}_n - \mathbf{p}_{\text{IRS}}|| < \frac{L}{2})$ [4]. We provide an illustrative example for this calculation in Section VI-A, where a WiFi scenario setup is evaluated.[5]

B. Transmission frame

Transmissions between the AP and the MU take place according to the frame structure depicted in Fig. 2, which

[3]We assume the circular geometry for the ease of evaluating the impact of MU mobility, as introduced later in Section IV-C1. We remark that this assumption does not limit the general model introduced in Section IV, which is independent of the geometry of the illuminated area.

[4]Hence, the activated IRS-elements resemble an IRS with circular shape. The indicator function is equal to 1, whenever the position of the IRS element is within the inscribed circle of the IRS, as follows from the condition $(||\mathbf{p}_n - \mathbf{p}_{\text{IRS}}|| < \frac{L}{2})$. We note that we adopt this strategy to have a simple mapping function. In principle, more sophisticated mapping functions or optimization-based designs can be developed to exploit the disconnected IRS elements.

[5]The Matlab code for the IRS coefficient implementation is provided in https://github.com/tkn-tub/IRS_Rejuvenation

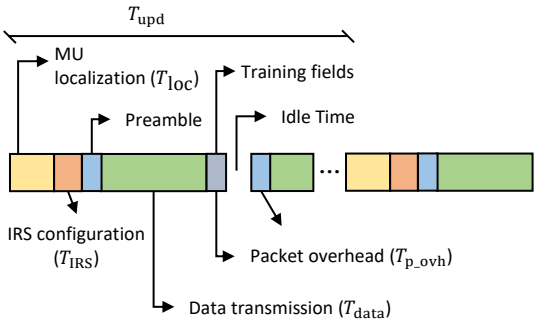

Fig. 2: Frame structure for IRS-assisted downlink transmission [27].

follows from [27]. Communication is performed in three phases. Firstly, the MU is localized by the AP along the time interval T_{loc}, as depicted within the first slot in Fig. 2. Using a given localization algorithm, the user is localized within the outer circle in Fig. 1.[6] Secondly, the IRS is configured in the time interval T_{IRS} to illuminate the MU. Thirdly, data transmission occurs per packet, where each packet comprises a preamble and a training field, as additional overhead along the interval $T_{\text{p\_ovh}}$, and the data in time interval T_{data}. Following this transmission scheme, the MU is localized, and the IRS reconfigured with the period T_{upd} when the MU's position is again updated, and the IRS reconfigured. Implicitly, we also assume there is always data to transmit in the available slots, and queues are not included as we consider a point-to-point link only.

Using this transmission scheme, the data communication period increases with the overhead introduced in time slots T_{loc}, T_{IRS}, $T_{\text{p\_ovh}}$ and the idle time (T_{idle}). The resulting overhead along the time interval T_{upd} can be evaluated as

$$T_{\text{ovh}} = T_{\text{loc}} + T_{\text{IRS}} + c_h(T_{\text{p\_ovh}} + T_{\text{Idle}}), \tag{6}$$

where

$$c_h = \left\lceil \frac{T_{\text{upd}} - (T_{\text{loc}} + T_{\text{IRS}})}{T_{\text{p\_ovh}} + T_{\text{data}} + T_{\text{Idle}}} \right\rceil, \tag{7}$$

is the number of packets emitted during T_{upd}, and $\lceil \cdot \rceil$ denotes the ceiling operation. Due to this overhead, the AP in the link can perform transmissions with the equivalent time

$$T_{\text{Tx}} = T_{\text{data}} + \frac{T_{\text{data}}}{T_{\text{upd}} - T_{\text{ovh}}} T_{\text{ovh}}. \tag{8}$$

The calculation in Eq. (8) accounts for the impact of overhead on the effective data transmission time. The second term in the sum above proportionally distributes the total overhead (evaluated with T_{upd}) among the total of data packets fitting within the time interval T_{upd}. This is evaluated as we divide T_{ovh} by the number of packets within T_{upd}, yielding $\frac{T_{\text{upd}} - T_{\text{ovh}}}{T_{\text{data}}}$. In practice, the AP performs a new packet transmission at periods larger than T_{data} and given by T_{Tx}.

[6]Localization algorithms that do not rely on IRS are surveyed in [28], whereas IRS-assisted localization schemes are reviewed in [29]. The design and analysis of the methodology proposed in this paper are independent of the specific adopted localization scheme.

C. Mobility model for the MU

As for the user's mobility, we assume the MU moves according to the random waypoint (RWP) mobility model [30]. In this model, the MU repeatedly selects a random destination point in a given area A (in our case, a circle of radius $r_{\text{out}} > r_{\text{in}}$, as depicted in Fig. 1) and moves with constant speed on a straight line between the departure and destination points. The random selection of the destination point follows a uniform probability distribution in the area. We also consider the case where the MU stops for a random time interval when reaching a destination and the case when the user moves at a random speed to the destination as well. We provide further details about the mobility models in Sections IV-C1 and IV-D.

IV. Modeling the Link Status as a Semi-Markov Regenerative Process

Before formulating the average PAoI, we provide insights into evaluating the fraction of time that the communication link is in any of the following three states:

i) Error-free transmission: This occurs when the MU is located in the illuminated area, i.e., inside the inner circle in Fig. 1.
ii) Transmission with error: This happens when the MU moves out of the illuminated region.
iii) Interruption of transmissions: Occurring when the IRS is being reconfigured.

These three states define all possible link statuses between the AP and the MU. We evaluate the fraction of time for each given state as the ratio between the duration of a given state to the update interval T_{upd}, yielding the portion of T_{upd} where the link is error-free, transmission with errors, or interrupted. Evaluating this fraction of time lets us to determine the average amplitude of the peaks in the AoI curve and, accordingly, the average PAoI that we formulate later in Section V.

The transition time instants between the above three states are generally a result of a random process. The MU stays in the illuminated area for a random amount of time as long as its corresponding waypoints are inside the inner circle in Fig. 1. However, depending on the periodicity of the IRS reconfiguration (T_{upd}), the MU will reach the outside area more or less quickly. It can also perform transitions between both areas due to the random mobility.

These transition patterns between areas are repeatedly generated during the MU localization phase, again starting the process regularly. The communication link will remain in a given state for a random time, except during the localization and IRS reconfiguration, where the link is interrupted (third state above) for a fixed amount of time ($T_{\text{loc}} + T_{\text{IRS}}$); see the transmission scheme in Fig. 2.

We model the dynamics of these three states by an MRGP [31, Sec. 10.6], allowing us to evaluate the time intervals of these states. In contrast to a pure Markov process, the MRGP model introduces random durations among transitions between states, allowing us to account for the random transition between error-free transmission and transmission with errors in the communication link. Besides, the MRGP model defines regeneration points, defined as those time instants where the

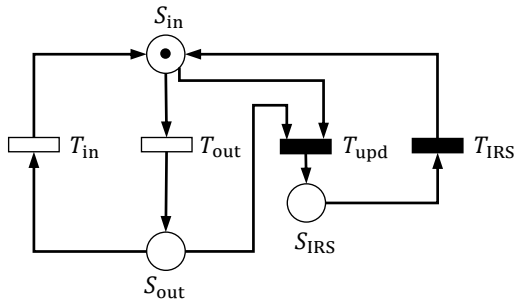

Fig. 3: Pictorial representation of the MRSPN.

random process replicates. In our case, the regeneration points are determined by the IRS reconfiguration, which will place the MU again inside the illuminated area, and the process repeats.

In contrast to a continuous-time Markov process, a Markov regenerative process relaxes the requirement of time independence. This requirement states that the waiting time for the next transition is independent of the time elapsed in the current state, which does not apply to the three states of the considered communication link; see [32, Eq. (12.1.13)]. In our current setup, the waiting time during MU localization and IRS reconfiguration is deterministic, while for the other two states (error-free transmission and transmission with error), the waiting time is random.

With the MRGP model, we follow a similar procedure as in [33], where a software system is periodically reset as preventive maintenance to subside failures. Analogously, in our case, the software components refer to the process running at the AP to implement the transmission scheme with the MU, i.e., localizing the MU, configuring the IRS, and performing transmissions. Failures are identified whenever the MU is not in the illuminated area, and maintenance corresponds with the MU localization and the IRS reconfiguration, after which the MU is again illuminated. This way, the communication process resembles a fault-tolerant system as in [33].

To derive the MRGP model, we follow the procedure in [33], where the evolution of the communication link is described first with a Markov regenerative stochastic Petri net (MRSPN) scheme. Then, we derive the reachability graph yielding the MRGP model representation, see also [34]. Finally, we evaluate the corresponding transition probabilities using the formulation of local and global kernels.

A. Stochastic Petri Net Representation

As depicted in Fig. 3, the Petri net (PN) representation allows for a graphical depiction of the flow of events [35] and also identifies the transition probabilities and regeneration points of the MRGP model [34]. As shown in Fig. 3, this representation ecompases the following features:

- The link status: Denoted with the three circles, also refered to as places, where S_{in} stands for the event when the node is in the illuminated area (error-free transmissions), S_{out} indicates that the node is outside the illuminated area (transmissions with errors), and S_{IRS} denotes the case when the node is localized and the IRS is reconfigured (no transmission happens).
- Transition between states: This is denoted with boxes, where the empty ones represent the random transitions between the states, while the filled boxes indicate the deterministic transitions.
- Connections between states and transitions: These connections are represented with directed arrows, providing direction among states.
- The current state of the link: This is denoted with a token, depicted with a dot. Fig. 3 depicts the initial condition in the link with the dot in the circle S_{in}, i.e., the node is in the illuminated area, and transmissions are error-free.

The boxes govern transitions between the circles (places) through the *firing* of events.[7] This firing refers to the boxes' activation; upon activation, the token at the input is moved to the box's output, representing the dynamic transition from the input to the output place. Furthermore, a box only enables the token's transition to the next state if a token is present at its input; otherwise, the firing does not occur. This representation also assumes that deterministic firing has priority over random firing. Whenever T_{upd} occurs, the token transitions from place S_{in} or S_{out} to S_{IRS}.

As the transition is governed by the MU location, the firing is accordingly defined with the following variables:

- T_{out}, a continuous stochastic variable indicating the MU transition from the illuminated area to the outer area in Fig. 1;
- T_{in}, a continuous stochastic variable indicating the MU transition from the outer area to the illuminated area;
- T_{upd}, a deterministic variable indicating the MU's position is updated while using a given localization algorithm (running at the AP); this firing occurs at regular time intervals;
- T_{IRS}, a deterministic variable indicating the IRS has been reconfigured and transmissions start again.

Given the firing rules, the evolution of the PN is described by the distribution of tokens at places S_{in}, S_{out}, and S_{IRS}. This distribution of tokens is defined by a vector, referred to as a mark [36], where each vector component is an integer number denoting the number of tokens at places S_{in}, S_{out}, and S_{IRS}. In the network in Fig. 3, there will be only three different marks as there are only a single token and three places. These marks are evaluated as follows: Departing from the initial mark, we have the vector $M_{\text{IRS}} = [1, 0, 0]$, denoting a single token is located at S_{IRS}. This mark denotes the case when the node is localized, and the IRS reconfigured. We evaluate the other two marks as $M_{\text{in}} = [0, 1, 0]$, indicating a token is located at S_{in}, and $M_{\text{out}} = [0, 0, 1]$ indicating the token is located at S_{out}. These two cases imply that the MU is within and outside the illuminated area, respectively.

Furthermore, the transitions of the token from one place to another can be represented by transitions between markers, which define the reachability graph as depicted in Fig. 4. This graph indicates which mark is reachable from the others according to the random (T_{in}, T_{out}) and deterministic (T_{upd}, T_{IRS}) firing of events. As a result of the process dynamics, all

[7]Within the Petri Net representation places refers to states, i.e., S_{in}, S_{out}, and S_{IRS} in Fig. 3.

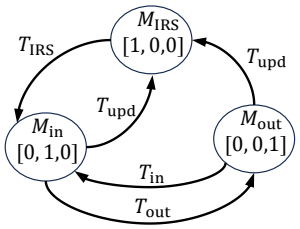

Fig. 4: Reachability graph of the MRSPN.

the marks are reachable from each other with a direct transition, except for M_{IRS}, which always transits to M_{in}.

B. Modeling the Link Dynamics using MRGP

The marks of the MRSPN readily define an MRGP; see [34, Theorem 2]. The state space of the underlying MRGP is directly given by the marks set as $\Omega = \{M_{\text{IRS}}, M_{\text{in}}, M_{\text{out}}\}$. The regenerative points are defined by the transitions to the state M_{IRS}, where the stochastic process restarts again with the MU mobility pattern. Consequently, the regenerative set comprises only a single element namely $\Omega' = \{M_{\text{IRS}}\}$.

The MRGP is completely described by the local and global kernels probabilities (see [34, Theorem 3]), which are defined as follows [33, Definition 2].

Global kernel $\mathbf{K}(t)$: This is an $m \times m$ matrix, where m is the cardinality of the regenerative set Ω' (in our case $m = 1$). The global kernel evaluates the process at the regeneration points (given by T_{upd}) with the conditional probability

$$\begin{aligned}\mathbf{K}(t) =&[K_{11}(t)] = [\Pr\{Z(T_{\text{upd}}) = M_{\text{IRS}}, T_{\text{upd}} \le t \,| \\ &\qquad |Z(T_0) = M_{\text{IRS}}\}], \\ =&[u(t - T_{\text{upd}})],\end{aligned} \tag{9}$$

where the Kernel's index "11" refers to state M_{IRS}, Z indicates the MU's state, T_0 denotes the initial time instant when the stochastic process starts, and $u(t)$ is the unit step function. We evaluate this conditional probability with the step function in (9), as the token is forced to return to place S_{IRS} at T_{upd}, and the condition $Z(T_{\text{upd}}) = M_{\text{IRS}}$ will occur with probability one whenever $t \ge T_{\text{upd}}$, see Fig. 3. In the meantime, the link is transitioning between S_{in} and S_{out}.

Local kernel $\mathbf{E}(t)$: This is an $m \times n$ matrix, where n is the cardinality of the state space Ω (in our case $n = 3$), that evaluates the behavior of the marks between two consecutive regenerative points. $\mathbf{E}(t)$ results in the 1×3 vector

$$\begin{aligned}\mathbf{E}(t) &= [E_{iq}(t)] = [\Pr\{Z(t) = Z_q, T_{\text{upd}} > t \,|\, Z(T_0) = Z_i\}], \\ &= \begin{bmatrix} E_{11}(t) & E_{12}(t) & E_{13}(t) \end{bmatrix}.\end{aligned} \tag{10}$$

where the lettered subscripts i and q denote the departing and arriving states, respectively, $i, q \in \{1, 2, 3\}$, and the corresponding Z's are $Z_1 = M_{\text{IRS}}$, $Z_2 = M_{\text{in}}$, and $Z_3 = M_{\text{out}}$. In Eq. (10), the entry $E_{11}(t)$ refers to the probability that the process running at the AP is in the localization and IRS configuration phases (denoted as M_{IRS}), given that the process always initiates at the same state M_{IRS}. This probability is readily obtained as

$$E_{11}(t) = 1 - u(t - T_{\text{conf}}), \tag{11}$$

with

$$T_{\text{conf}} = T_{\text{loc}} + T_{\text{IRS}}. \tag{12}$$

This formulation states that the MU will remain with probability one in the M_{IRS} state along time interval $[0, T_{\text{conf}}]$, whenever T_{upd} triggers.

The term E_{12} evaluates the probability that the process continues to be in M_{in} before the first regeneration point T_{upd}. We recall that M_{IRS} denotes the localization and IRS configuration processes, after which the MU is again illuminated. Thereby, the token will be at place S_{in} immediately after T_{IRS} and will stay within the illuminated area with probability P_{in} till the next regeneration point. Evaluating these two conditions together yields

$$E_{12} = \begin{cases} 0 & \text{when } t \le T_{\text{conf}} \\ 1 & \text{when } T_{\text{conf}} < t \le \frac{r_{\text{in}}}{v} \\ \mathrm{P}_{\text{in}}(t - t_0 < T_{\text{upd}}) & \text{when } t > T_{\text{conf}} \end{cases} \tag{13}$$

where $\mathrm{P}_{\text{in}}(t < T_{\text{upd}})$ denotes the probability that the MU remains inside the inner circle till the next regeneration point T_{upd}. In Section IV-C we evaluate the probability that the MU leaves the illuminated circular area departing from an arbitrary location within the circle, here denoted with $\mathrm{P}_{\text{in}}(t < T_{\text{upd}})$. As we assume that the localization phase centers the circle of the illuminated area in the MU position, see Fig. 1, we introduce the time shift $t_0 = T_{\text{conf}} - \frac{r_{\text{in}}}{v}$ accounting for the initial MU's location in the circle center instead, where $\frac{r_{\text{in}}}{v}$ accounts for the minimum time the MU takes to travel from the the center of the illuminated area to the outside area. This probability ultimately depends on the MU's mobility pattern. We illustrate the calculation and the validation of this probability in Section IV-C for various RWP mobility models.

Similarly, E_{13} is evaluated as follows

$$E_{13}(t) = \mathrm{P}_{\text{out}}(t - T_{\text{conf}} < T_{\text{upd}})u(t - T_{\text{conf}}), \tag{14}$$

where $\mathrm{P}_{\text{out}}(t < T_{\text{upd}})$ denotes the probability that the MU stays in the outer area and assuming the MU's initial position is in the same outer area. In this equation, we introduce the time shift T_{conf} as this event always occurs after the IRS is reconfigured. We evaluate this probability in Section IV-E.

The two kernels in (9) and (10) allow us to evaluate the steady-state transition probability, as [33, Eq. (5)]

$$\pi_q = \frac{\sum_{k\in\Omega} p_k \alpha_{kq}}{\sum_{k\in\Omega} p_k \sum_{l\in\Omega} \alpha_{kl}}, \tag{15}$$

where $q \in \{1, 2, 3\}$ denotes three link states, namely IRS reconfiguration, error-free transmission, and transmision with errors, respectively. Moreover, $\alpha_{k,q}$ is given by

$$\alpha_{kq} = \int_0^\infty E_{kq}(t)\mathrm{d}t, \tag{16}$$

and p_k in Eq. (15) are the components of $\mathbf{p}$ as a $1 \times n$ vector, which is the solution to the equation

$$\mathbf{p} = \mathbf{p}\mathbf{K}(\infty), \tag{17}$$

under the condition $\sum_{i\in\Omega'} p_i = 1$. As this condition states that $p_1 = 1$ (there is only a single regeneration state as M_{IRS}), and $\mathbf{K}(\infty) = 1$ (see Eq. (9)), the evaluation of (17) yields the

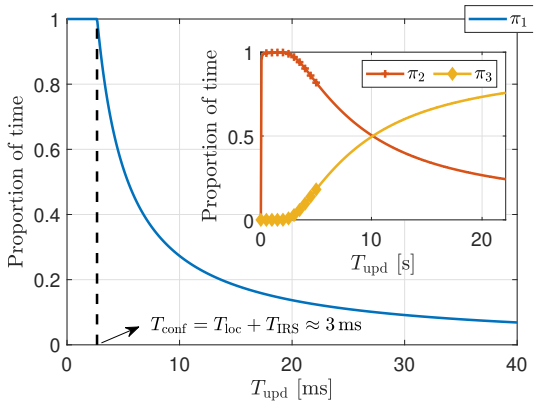

Fig. 5: Fraction of time (see (18)) for the three states in the link considering $r_{\text{in}} = 1.7\,\text{m}$, $r_{\text{out}} = 3\,\text{m}$, and mobility of constant speed $v = 1\,\text{m/s}$ without stop time.

trivial solution $\mathbf{p} = [1\,0\,0]$. Replacing this solution into (15) finally evaluates π_j as

$$\pi_q = \frac{\alpha_{1,q}}{\sum_{l\in\Omega}\alpha_{1,l}}, \tag{18}$$

By definition, π_q in (18) provides the proportion of time the token is on each place with respect to the time interval between regeneration points (see [34, Theorem 6]). In our case, it refers to the proportion of time the link is in either of the above-mentioned states: transmitting error-free, transmitting with errors, or non-transmitting. We will use this equation to evaluate the average PAoI in Section V.

The proportion of time vector π_q will ultimately depend on the probability that the MU is inside the illuminated area (P_{in}), outside (P_{out}), and the amount of time needed to localize and reconfigure the IRS (T_{conf}). To illustrate, Fig. 5 depicts the fraction of time for the three communication link states after numerically evaluating (18), and using the calculations made in the next sections for the probabilities P_{in} and P_{out}. We choose to illustrate assuming the RWP mobility model with speed $1\,\text{m/s}$ for the MU and with the inner radius of the illuminated area as $1.7\,\text{m}$; this is the illuminated area where the IRS-assisted link evaluates no packet errors (evaluated later in Section VI). The link is with probability one ($\pi_1 = 1$) in the localization and reconfiguration phases whenever $T_{\text{upd}} \leq (T_{\text{loc}} + T_{\text{IRS}})$ and starts to decrease afterward. As T_{upd} increases, the MU reduces its probability to stay inside the illuminated area (π_2). Eventually, the MU starts to spend time in the outer area with increased probability, which follows the curve π_3. In the following, we provide the calculations for P_{in} with the RWP mobility model. A similar procedure will follow to evaluate P_{out}.

C. Evaluating the Probability for MU to Stay Inside the Illuminated Area

We evaluate the probability for error-free transmissions as the probability that the MU stays inside the illuminated area (denoted as P_{in} in (13)). To evaluate this probability, we first compute the first-hitting-time probability [37] that the MU reaches the outer area in Fig. 1. Denoting this probability as $P_{\text{fh\_out}}(t)$, we readily compute $\text{P}_{\text{in}}(t)$ as

$$\text{P}_{\text{in}}(t) = 1 - P_{\text{fh\_out}}(t). \tag{19}$$

Following the RWP mobility model, we decompose the calculation of $P_{\text{fh\_out}}$ into two steps. In the first step, we compute the probability for the MU to leave the inner circle, see Fig. 1, with the first-hitting time probability. We evaluate the probability for the number of consecutive waypoints inside the inner circle before the MU transitions to the outer area. In the second step, we evaluate the probability of the elapsed time between waypoints in the inner circle and add those random variables. The sum provides a close estimate of the total time the MU spends within the illuminated area, resulting in $\text{P}_{\text{in}}(t)$. We illustrate this approximation later with Section IV-D and graphically in Fig. 6.

1) First-hitting time probability: To evaluate this probability, we need to compute the survival probability first; which evaluates the probability for the MU to stay in the inner circle for j-consecutive waypoints. Here denoted as S_j, this evaluation introduces the impact of the particular geometry of the illuminated area, in our case a circle of arbitrary radius r_{in}. The probability of selecting a waypoint in the inner circle of area A_{in} is directly given as $p = \frac{A_{\text{in}}}{A}$, where A denotes the area of the outer circle in Fig. 1. In this way, the value for p inherently evaluates equal probability of displacing to any point in A, following the RWP model; see [30]. Consequently, the probability that the MU selects j-consecutive waypoints within the inner circle yields the survival probability $S_j = \left(\frac{A_{\text{in}}}{A}\right)^j$, $j \geqslant 0$, as each waypoint selection is independently performed. Given S_j, the first-hitting probability is readily evaluated as [37]

$$P_{J\text{out}}(j) = S_J(j) - S_J(j+1) = \left(\frac{A_{\text{in}}}{A}\right)^j \left(1 - \frac{A_{\text{in}}}{A}\right), \tag{20}$$

$$\frac{A_{\text{in}}}{A} \in (0,1),\ j \geqslant 0,$$

which represents the first-hitting time probability in the discrete space of jumps, and J_{out} is a random variable denoting the waypoint where the MU is for the first time outside the illuminated area.

2) First-hitting time probability in the time-space: For each performed jump, the MU moves a random distance l_j with a given speed v, where the probability density function (PDF) for l_j is given as [30, Eq. (23)]

$$f_L(l_j) = \frac{8}{\pi r_{\text{in}}}\frac{l_j}{2r_{\text{in}}}\left(\arccos\left(\frac{l_j}{2r_{\text{in}}}\right) - \frac{l_j}{2r_{\text{in}}}\sqrt{1-\left(\frac{l_j}{2r_{\text{in}}}\right)^2}\right). \tag{21}$$

We evaluate (21) considering the MU displaces in the inner circle only, as we aim to evaluate the elapsed time interval before the MU leaves it. For this case, we assume $l_j \in [0,\, 2r_{\text{in}}]$, where r_{in} denotes the radius of the inner circle in Fig. 1.

Using the formulation in Eq. (21), we can consider three different cases for the MU mobility pattern. In the first case,

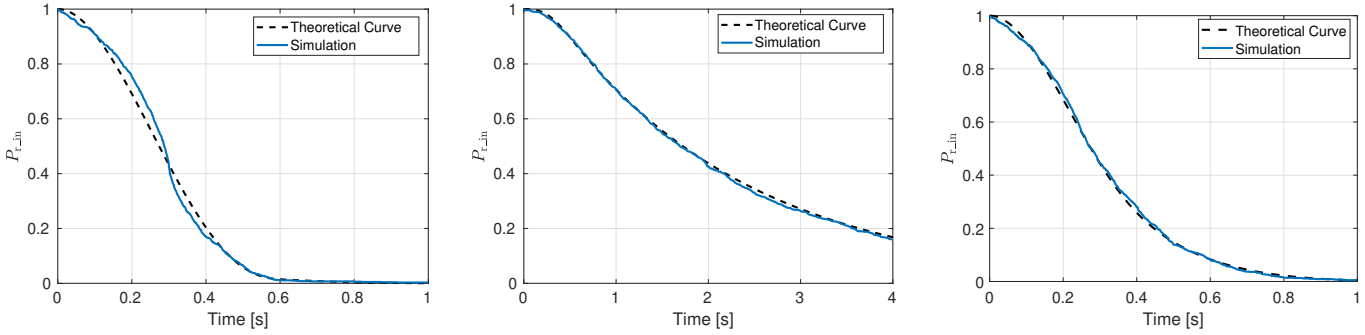

(a) RWP mobility model when the MU displaces with constant speed $1\,\mathrm{m/s}$, without stop time.

(b) RWP mobility model with random stop time following an exponential distribution $f_{T_p}(\tau) = \mu e^{-\mu\tau}$ and mean waiting time $\mu = 2\,\mathrm{s}$.

(c) RWP mobility model when the MU displaces with random speed based on the uniform distribution between $v_{\min}$ and $v_{\max}$, where $v_{\min} = 0.5\,\mathrm{m/s}$ and $v_{\max} = 1.5\,\mathrm{m/s}$.

Fig. 6: Validation for the P_{in} in (19) with simulation of the RWP mobility for inner circle radius $1\,\mathrm{m}$. The exponential distribution in b) follows [30, Example in page 561], the uniform distribution in c) follows [30, Sec. 3.5.1].

the MU moves with constant speed v between waypoints along the time interval $\tau_j = \frac{1}{v} l_j$, where (see [30, Eq. (28)])

$$f_{\tau_j;r_{\mathrm{in}}} = v f_L(v\tau_j),\ \tau_j \in \left(0,\ \frac{2r_{\mathrm{in}}}{v}\right) \tag{22}$$

In the second case, the MU performs a random pause time T_p with PDF $f_{T_p}(t_p)$, yielding [30, Eq. (39)]

$$f_{\tau'_j;r_{\mathrm{in}}} = \int_0^{\tau'} f_{\tau_j;r_{\mathrm{in}}}(\tau) f_{T_p}(\tau' - \tau)\mathrm{d}\tau. \tag{23}$$

In the last case, the MU displaces at a random speed v following $f_V(v)$ as the PDF, yielding [30, Eq. (39)]

$$f_{\tau'_j;r_{\mathrm{in}}} = \int_{v_{\min}}^{v_{\max}} v f_{\tau_j;r_{\mathrm{in}}}(\tau) f_V(v)\mathrm{d}v. \tag{24}$$

We approximate the total time elapsed till the MU displaces out of the inner circle as the sum of the time intervals along J-consecutive waypoints except for the last one as[8]

$$T_{\mathrm{out}} \approx \sum_{j=1}^{J_{\mathrm{out}}-1} \tau_j, \tag{25}$$

where J_{out} is a random variable denoting the waypoint when the MU leaves the inner circle for the first time, see for instance the case depicted in Fig. 1 where $J_{\mathrm{out}} = 3$.

To provide a formula for the probability that the MU leaves the inner circle for the first time before T_{upd}, we use the formula for the total probability, yielding [38]

$$P_{\mathrm{fh\_out}}(t) = \sum_{j=1}^{\infty} P(T_{\mathrm{out}}|j) P_{J\mathrm{out}}(j), \tag{26}$$

as (25) is the sum of an arbitrary amount of random variables τ_j, where $P(T_{\mathrm{out}}|j)$ denotes the probability for the total elapsed time along j-jumps, evaluated through the corresponding PDF[9]

$$f_{T_{\mathrm{out}}}(t_{\mathrm{out}}|j) = \underbrace{f_{\tau_j;r_{\mathrm{in}}} * \cdots * f_{\tau_j;r_{\mathrm{in}}}}_{j}\Big|_{\tau_j = t_{\mathrm{out}}}, \tag{27}$$

where $f_{\tau_j;r_{\mathrm{in}}}$ is obtained using Equations (22) to (24) depending on the mobility model.[10] This relation is evaluated numerically as no closed-form expression exists for the N-fold convolution of any of the functions in Eqs. (27). To summarize, we evaluate the probability of the MU leaving the inner circle for the first time with (26), where $P_{J\mathrm{out}}(j)$ as given by (20) and $P(T_{\mathrm{out}}|j)$ is evaluated numerically by integrating the PDF in Eq. (27).

D. Validating the Theoretical Expression for $\mathrm{P_{in}}(t)$

We validated the theoretical expressions for the $\mathrm{P_{in}}(t)$ in (19) through simulations. We evaluated the probability after 1000 realizations accounting for the time instant when the MU leaves the inner circle for the first time. We simulated the three mobility models tracking the position of the MU and recorded the time when the MU leaves the inner area, giving the results illustrated in Fig. 6 for the three different models in Equations (22) to (24). The theoretical formulation for $\mathrm{P_{in}}$ in (19) manifests a good correspondence with the simulation of the three RWP mobility models as illustrated in Fig. 6.

E. Evaluating the Probability that the MU Stays Outside of the Illuminated Area

To evaluate the probability that the MU stays outside the illuminated area, we follow the same procedure as in Section IV-C. We compute the first-hitting time at which the MU reaches the inner circle $P_{\mathrm{fh\_in}}$ when initially being in the outer area, and evaluate the probability for the MU to remain in the outer circle as

$$\mathrm{P_{out}}(t) = 1 - P_{\mathrm{fh\_in}}(t). \tag{28}$$

To compute $P_{\mathrm{fh\_in}}$, we evaluate the survival probability as in Eq. (20), just replacing A_{in} with $(A - A_{\mathrm{in}})$. Then, to evaluate $P_{\mathrm{fh\_in}}(t)$, we use the same formulation for the total probability as in (26), but replacing T_{out} with T_{in}. Besides, $P(T_{\mathrm{in}}|j)$ is evaluated with its corresponding PDF, similarly formulated as in (27), after replacing r_{in} with r_{out}, to evaluate $f_{\tau_j;r_{\mathrm{out}}}$. We

[8]This approximation is a pessimistic calculation for the elapsing time inside the illuminated area. The exact time is larger, and it evaluates the time interval just when the MU intercepts the perimeter of the illuminated area.

[9]As the elapsing time is the sum of independent time intervals between jumps (see (25)), its corresponding PDF can be evaluated using the N-fold convolution of f_{τ_j}; see [38].

[10]Evaluating (27) as the convolution implicitly assumes the MU starts at a random position inside the inner circle.

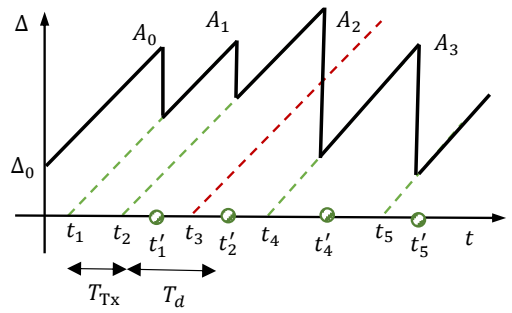

Fig. 7: Illustration of the AoI of packets (dashed lines) and as perceived on a given destination node (bold line).

note that, following these calculations, we implicitly assume the worst-case scenario, thus avoiding the calculation of possible interceptions between the MU trajectory and the illuminated area.

V. AoI Framework

In the following, we theoretically formulate the average PAoI metric to balance the overhead and data transmission time slots. We aim to evaluate the update period of the IRS, with the value of T_{upd} in Fig. 2, and balance the trade-off between overhead and transmission opportunities. The more frequently we update the IRS (smaller T_{upd}), the higher the chances of error-free transmissions, as the MU will be mostly in the illuminated area. However, with the increased update frequency, the overhead becomes larger, thereby limiting the availability of time slots to transmit data. Conversely, reducing the frequency of updates (increased T_{upd}) allows more time slots for transmission. Yet, this is at the expense of more errors and less throughput, as the MU will increasingly spend more time outside the illuminated area between IRS updates. Such a dynamic behavior evidences a trade-off between overhead and throughput that we aim to balance with the AoI framework in this section.

The PAoI metric results from the sequence of peaks in the AoI curve, which is evaluated based on the generation $(t_{i+1} - t_i)$ and system $(t'_i - t_i)$ times, where t_i denotes the time instant when a packet is generated, and t'_i is the time when it is successfully received; see their representation in Fig. 7.[11] Following the illustration in this figure, the AoI curve is the continuous line and the PAoI refers to the sequence of peaks A_i. The AoI curve will linearly increase between consecutive receptions (e.g., between t'_1 and t'_2) following the increasing age of the most recent received packet (e.g., at t'_1). As a result, the AoI is a sawtooth curve with peaks $\{A_0, A_1, \dots\}$ representing the highest age at the reception time. The average PAoI, denoted as $\Delta^{(p)}$, corresponds to the average of the sequence of peaks and is evaluated as

$$\Delta^{(p)} = \mathbb{E}[A_i] = \mathbb{E}[T_g] + \mathbb{E}[T_s] \tag{29}$$

as follows from [39, Def. 3.3.2], where $T_g = t_{i+1} - t_i$ denotes the generation time, and $T_s = t'_i - t_i$ is the system time.

[11]This definition follows [11] and [39, Def. 3.1].

A. Integrating the System Model within the AoI Concept

Although Eq. (29) is not that explicit *per se*, the height of the peaks in the AoI directly reflects the dynamics in the communication link. We substantiate this statement through the following facts:

- The transmission time in the downlink (T_{Tx} in (8)) corresponds to the time interval between the generation of two successive packets in the AoI formulation, i.e., the generation time $(t_{(i+1)} - t_i)$ is equal to T_{Tx}; see the illustration in Fig. 7. Besides, as T_{Tx} also accounts for the communication overhead and the latency (due to the packet size) in the link, the generation time also conveys the same two components (overhead and latency); see the dependency of T_{Tx} with T_{ovh} and T_{data} in (8).
- The two link conditions, error-free transmission and transmission with errors, are included within the system time $(T_s = t'_i - t_i)$. When the link is error-free, the system time is the minimum possible and equal to the transmission delay, e.g., $t'_2 - t_2 = T_d$; see Fig. 2. However, when the link causes errors, the system time increases until the MU returns to the area illuminated by the IRS or the IRS is again reconfigured to illuminate the MU. In this regard, the system time is a random variable that depends on the size of the illuminated area (defined by the IRS), the mobility pattern of the MU, and the update period of the IRS.
- As a result of the above interrelation of the generation and system times with the system model parameters, the impact of the transmission overhead, IRS reconfiguration, and mobility is jointly evaluated within the amplitude of the peaks in the AoI curve, as directly follows from Eq. (29). In this way, the average PAoI metric accounts for the overhead and the dynamics of the communication link between interruption of transmissions, errors-free transmission, and transmission with error.
- Finally, the average PAoI metric is minimized based on the IRS update period (T_{upd}), allowing us to optimally balance the impact of overhead and throughput in the link.

In the next section, we elaborate on a closed-form expression for the average PAoI metric and illustrate the optimal IRS update period.

B. Closed-form expression for the average PAoI

To obtain a closed-form expression for $\Delta^{(p)}$, we consider the temporal evolution of the AoI curve in Fig. 7. The evolution of the AoI curve follows the dynamic of the communication system according to the three states illustrated in Fig. 4. The corresponding height of the peaks can be evaluated for these three different cases as follows:

Case 1 (IRS is reconfigured): This is the initial state, where the MU is localized and the IRS is reconfigured; see Fig. 2. In this state, transmissions are interrupted along the time interval $T_{\text{conf}} = T_{\text{loc}} + T_{\text{IRS}}$. This case is already included within the transmission time interval T_{Tx} in Eq. (8); see the dependency of the T_{ovh} term with $(T_{\text{loc}} + T_{\text{IRS}})$ in Eq. (6).

Case 2 (MU is inside the illuminated area): In this case, errors do not occur, and the height of the peaks can readily be evaluated as

$$A_{i,\text{in}} = T_d + T_{\text{Tx}}, \tag{30}$$

along the time interval inside the illuminated area, where $T_d = \frac{c}{d}$ is the communication delay between the MU and the AP, c is the speed of light and d is the sum of the distances between the MU and the IRS and between the IRS and the AP. The relation in (30) computes the time elapsed between two consecutive receptions [40]; see for example the reception at t'_1 and t'_2 in Fig. 7, where $T_{\text{Tx}} = t_{i+1} - t_i$ and $T_d = t'_i - t_i$ are assumed to be deterministic variables. This event (amplitude of the peaks) will occur with the steady state probability $\pi_j|_{j=2}$ as a result of evaluating (18).

Case 3 (MU is outside the illuminated area): In this case, packets are not decoded and thereby dropped, leading to an increase of the AoI. See the case depicted in Fig. 7, where the packet at t_3 is not received, and the age increases till the reception of the next emitted packet at t'_4. Specifically, the peak AoI increases by the amount T_{Tx}, i.e., as $(T_{\text{Tx}} + T_{\text{data}} + T_{\text{Tx}})$, as the receiver must wait to create the next packet at t_4. When considering an arbitrary time interval for the MU to stay outside the illuminated area, denoted as T_{o}, the waiting time before the next packet arrives yields $\left\lceil \frac{T_{\text{o}}}{T_{\text{Tx}}} \right\rceil \times T_{\text{Tx}}$. In this way, the corresponding peak in the AoI curve is readily evaluated as

$$A_{i,\text{out}} = T_d + T_{\text{Tx}} + \left\lceil \frac{T_{\text{o}}}{T_{\text{Tx}}} \right\rceil T_{\text{Tx}}, \tag{31}$$

occurring with the steady state probability $\pi_j|_{j=3}$ as a result of evaluating Eq. (18). This formulation implicitly assumes that errors will happen independently of the time duration outside the illuminated area, i.e., as long as $T_{\text{o}} > 0$.

We evaluate the average PAoI based on Cases 2 and 3, as we consider the overhead from the first case already introduced in the formulation for T_{Tx} as in (8). For this evaluation, we use the fraction of time relative to the time interval for transmissions only, i.e., after the localization and reconfiguration phases along the time interval $(T_{\text{upd}} - T_{\text{loc}} - T_{\text{IRS}})$; see Fig. 2. Accounting for the inclusion of $T_{\text{conf}} = T_{\text{loc}} + T_{\text{IRS}}$ within the Cases 2 and 3, we proportionally increase both probabilities π_2 and π_3 with $(\pi_2\pi_1)$ and $(1-\pi_2)\pi_1$, respectively, as these terms evaluate the fraction of time (given by $\pi_2\pi_1$ in Case 2) of transmissions that proportionally includes T_{conf}, as provided by $(\pi_2 + \pi_2\pi_1)T_{\text{upd}}$. These evaluations yield the following probabilities

$$\begin{aligned} \pi'_2 &= \pi_2 + \pi_2\pi_1 \\ \pi'_3 &= \pi_3 + (1-\pi_2)\pi_1, \end{aligned} \tag{32}$$

complying with the relation $\pi'_2 + \pi'_3 = 1$. Then, using (30) and (31) and evaluating the average time that the MU is outside the illuminated area as $T_{\text{o}} = \pi_3 T_{\text{upd}}$, we can calculate the average PAoI as

$$\begin{aligned} \Delta^{(p)} &= A_{\text{in}} \times \pi'_2 + A_{i,\text{out}}\big|_{T_{\text{o}}=\pi_3 T_{\text{upd}}} \times \pi'_3, \\ &= (T_d + T_{\text{Tx}}) \times (\pi'_2 + \pi'_3) + \left\lceil \frac{\pi_3 T_{\text{upd}}}{T_{\text{Tx}}} \right\rceil T_{\text{Tx}} \times \pi'_3, \\ &= (T_d + T_{\text{Tx}}) + \left\lceil \frac{\pi_3 T_{\text{upd}}}{T_{\text{Tx}}} \right\rceil T_{\text{Tx}} \times \pi'_3. \end{aligned} \tag{33}$$

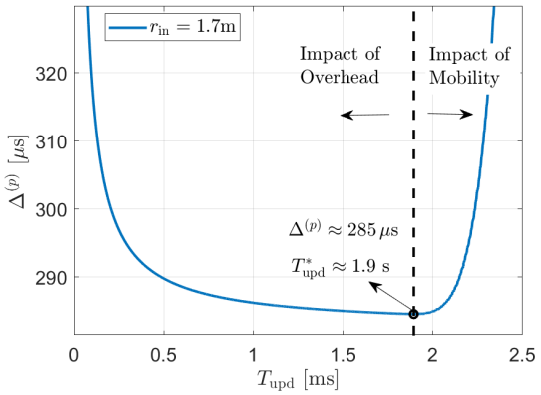

Fig. 8: Resulting average PAoI assuming the RWP mobility model with $v = 1\,\text{m/s}$ for the MU, $r_{\text{in}} = 1.7\,\text{m}$, and outer radius $r_{\text{out}} = 3\,\text{m}$.

Eq. (33) jointly accounts for the impact of the overhead and communication errors. The overhead is included in T_{Tx} (see (8)), while the communication errors are accounted for in the terms π_3 and π'_3, as these two probabilities reflect the case when the MU is outside the illuminated area. To illustrate these two mechanisms, we depict the impact of the two mentioned components in Fig. 8. Reducing T_{upd} will increase the AoI as the overhead increases. Conversely, increasing T_{upd} will also increase the age of information as the MU will spend time outside the illuminated area with increasing probability. In the next section, we provide more insights into this calculation and its practical use to balance the overhead introduced by the IRS in the communication link.

VI. Results: Balancing the Impact of the Overhead and Packet Losses for a WiFi Scenario

This section illustrates the application of the above theoretical formulation and studies the optimal reconfiguration periodicity for the IRS. The optimal balance is attainable by minimizing the expression in Eq. (33); however, its evaluation is not straightforward as we need first to evaluate its dependency on the probabilities π'_2, π'_3 and π_3 within the application scenario. We also need to evaluate the dependency of the average PAoI metric with T_{upd}, T_{Tx} and T_d according to the communication protocol and the communication distances. For this evaluation, we choose a functional scenario where we implement a communication link over WiFi in the mmWave band.[12] We illustrate the average PAoI metric for a communication system compliant with the IEEE 802.11ad standard and provide realistic performance values.

[12]Other particular communication scenarios (as in fifth generation (5G)) are also applicable as long as they follow a packet-format scheme as illustrated in Fig. 2.

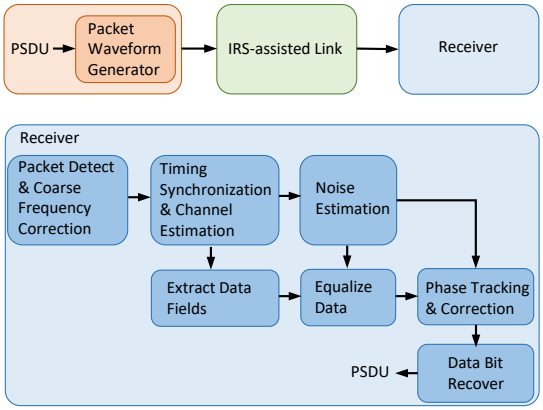

Fig. 9: Block diagram for the implemented transmission-reception scheme according to the 802.11ad.

A. Scenario Setup

We follow the IEEE 802.11ad standard as it operates in the mmWave band [41] through the schematic in Fig. 1. The communication link consists of a single AP-MU link through the IRS-assisted channel; where we assume NLOS conditions between the AP and the MU. In this communication link, we locate the AP at $2.5\,\mathrm{m}$ height from the floor, and MU's terminal is located at $1.5\,\mathrm{m}$ height. The communication between the AP and the MU occurs through the IRS located in the ceiling at a height of $3\,\mathrm{m}$, where the MU is within the near field region of the IRS.

The AP generates a random data sequence and creates an IEEE 802.11ad packet with the preamble and data field length, as listed in Table I.[13] We perform transmissions with the modulation and coding scheme (MCS) 12.6, which corresponds to a single-carrier 64-quadrature amplitude modulation (QAM), encoded with a low-density parity-check (LDPC) code; see [42, Table 20.19 and Sec. 20.6.3.1.4].[14]

As illustrated in Fig. 1, the signal travels from the AP to the IRS, and from there, it is reflected to the ground plane where the MU is located. We abstract the communication link with the SNR parameters as evaluated in Eq. (1), where $\lambda = \frac{c}{f_c} \approx 5\mathrm{mm}$ corresponds to the center frequency of transmissions $f_c = 60.48\,\mathrm{GHz}$. This transmission frequency is the selected carrier frequency for channel two within the 802.11ad standard and is available in all regions. The receiver decodes the information bits in the data field after various signal processing blocks accounting for packet detection, time and frequency synchronization, and channel and noise estimation. See details in the block diagram representation of the link and the receiver in Fig. 9. The transmission and noise power levels at the receiver are selected from the ETSI report in [44] and listed in Table I.

[13]For details on the IEEE 802.11ad packet structure, we refer to the directional multi-gigabit (DMG) PHY implementation, as given within the standard in [42, Sec. 20]. A summary of these parameters is also listed in [43].

[14]MCS $= 12.6$ enables high throughput transmissions ($8\,\mathrm{Gbit/s}$) and large data packets ($\approx 262\,\mathrm{kB}$ per frame) supporting applications like 3D high-definition video streams. This setting affords transmissions in long-lasting channel coherence times; which is the case in our scenario where the MU speed is not larger than $1\,\mathrm{m/s}$.

TABLE I: Simulation parameters.

	Variable	Description	Value
Frame parameters		Preamble field length	4352 samples
		Maximum data field length	456 768 samples $\approx$ 262 kB
		Training field length	3712 samples
		Idle time	20 µs
	MCS	Modulation and coding scheme	12.6
	N	Total of IRS reflecting elements	160×160
RF parameters	f_s	Sampling rate	1.76 GHz
	BW	Receiver bandwidth	2640 MHz
	f_c	Carrier frequency, corresponding to Channel 2	60.48 GHz
	P_{Tx}	Transmitter peak power	30 dBm
		Number of AP antennas	8
		Number of AP beams	4
		Gain per AP beam	9 dBi
	NF	Noise figure	7 dB
	N_0	Thermal noise density	$-174\,\mathrm{dBm/Hz}$
	$\mathrm{N}_{\mathrm{int}}$	Receiver interference density	$-165.7\,\mathrm{dBm/Hz}$
	P_{N}	Noise floor	$\approx -70\,\mathrm{dBm}$
	$\mathbf{p}_{\mathrm{AP}}$	AP's location	[2, 0, 2.5] [m]
	$\mathbf{p}_{\mathrm{IRS}}$	IRS's location	[2, 3, 3] [m]
	$\mathbf{p}_{\mathrm{MU}}$	MU's initial location	[2, 3, 1.5] [m]
	v	MU's speed	1 m/s

The parameters for the length of the preamble, data field, and training subfield follow the IEEE 802.11ad PHY frame parameters and are quantified within the Matlab code in [45]. The preamble field encompasses the short training, channel estimation; and header fields. The training subfields encompass the automatic gain control and beamforming training fields; see [43].
We follow the ETSI report in [44, Table 5, entries (13) to (17) pp. 51] to define the noise-related values. We evaluate the noise floor as $P_{\mathrm{N}} = 10\log(10^{\frac{\mathrm{NF}+N_o}{10}} + 10^{\frac{N_{\mathrm{int}}}{10}}) + 10\log(\mathrm{BW})$. Regarding the IRS, we choose 160×160 elements, equivalently to a size of $160 \times \frac{\lambda}{2} = 160\frac{c}{2f_c} \approx 40\,\mathrm{cm}$, where c is the speed of light. We choose this value as we observe a sufficiently high SNR in the center; see Fig. 10. An example of fabricated solutions is 160×160 in the 60 GHz band [46].

We configure the IRS of 160×160 elements as indicated in Section III-A. We selected the IRS dimension as follows from the fabricated module in [46]. To ensure seamless communication for the MU, we configure the IRS to render an SNR larger than $30\,\mathrm{dB}$ within the illuminated area. There, we observe zero bit error rate (BER) for encoded transmissions. Following this setup, the IRS projects a nearly circular SNR pattern on the ground since it is installed in the ceiling; see Fig. 10. The results presented in Fig. 10 assure the largest illuminated area for the corresponding SNR value larger than $30\,\mathrm{dB}$ with a wide-beam parameter of $\Delta x = \Delta y = 1.7$ m. As depicted in Fig. 10, outside the illuminated area, the MU experiences lower SNR values, as the beam from the AP is steered by the IRS mainly to inside the area.

B. Evaluating the Transmission Frame Parameters

We evaluate the variables T_{IRS}, T_{loc}, $T_{\mathrm{p\_ovh}}$, and T_{data} using the parameters listed in Table I as follows:
IRS reconfiguration (T_{IRS}): We assume the IRS is equipped with a WiFi interface, and the AP sends the pre-calculated IRS coefficients, as introduced in Section VI-A, through this interface. Although the coefficients can be calculated at the IRS, we select to be evaluated at the AP in favor of reduced

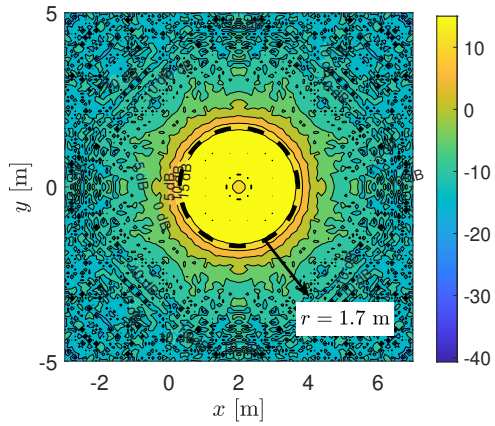

Fig. 10: Heat map of the SNR values for the IRS's illuminated area and the parameters given in Table I, following the framework presented in [26].

computational complexity with the IRS equipment. In this setup, we also assume that the reconfiguration time equals the transmission time of a WiFi packet, where the data block within the frame is of the minimum length needed to send the coefficients from the AP to the IRS. Assuming a double point precision of 32 bits per coefficient, and that the IRS comprises 160×160 coefficients (see Table I), the amount of bytes needed is $\text{Data}_{\text{IRS}} = \left\lceil \frac{32 \times 160^2}{8} \right\rceil = 102.4\,\text{kB}$ yielding

$$\begin{aligned} T_{\text{IRS}} &= T_{\text{PPDU-IRS}}, \\ &= \frac{1}{f_s}(\text{Preamble field length + Data}_{\text{IRS}} \\ &\quad + \text{Training field length}), \\ &\approx 105.4\,\mu\text{s}, \end{aligned} \tag{34}$$

This calculation follows the physical layer protocol data unit (PPDU) structure, according to the IEEE 802.11ad standard (see details in [43]). The preamble, training lengths, and sampling frequency f_s are specified in Table I while Data_{IRS} is evaluated as already indicated above.[15]

Localization time (T_{loc}): We follow the solution reported in [29] for localization, where an IRS is reconfigured to scan the MU plane and look for its reflected signals in a WiFi scenario.[16] The method performs once a coarse-grained measurement to obtain the initial position of the MU and continues tracking the user with fine-grained measurements. The fine-grained measurement is the one we account for with the localization time, as the coarse-grained measurement is performed only once, yielding negligible associated overhead over time. For the fine-grained measurement, a 1×1 m^2 area around the MU location is divided into 11×11 blocks; see [29, Sec. VI A]. The IRS is reconfigured once per block by the AP, and then measurements are performed with the AP sending two data packets per block via the IRS. Adopting this approach and setup, the localization time yields

$$\begin{aligned} T_{\text{loc}} =& (2 \text{ transmissions}) \times (11^2 \text{ blocks}) \times T_{\text{PPDU-loc}} + \\ &+ (11^2 \text{ blocks}) \times T_{\text{PPDU-IRS}} \\ \approx& 15\,\text{ms}, \end{aligned} \tag{35}$$

where the first term accounts for the transmission of two packets per block, and the second term for the IRS reconfiguration per block. The parameter $T_{\text{PPDU-IRS}}$ is calculated similarly as in (34) but with $\text{Data}_{\text{loc}} = 1$, which refers to the transmission of a single byte within the data block in the frame.[17] We remark that Eq. (35) only reflects time slots for packet transmissions, as we assume that the computation time required to run the localization algorithm is negligible when compared to the transmission time. The implicit assumption is that the computational capabilities at the AP are sufficiently high.

Preamble and training time ($T_{\text{p\_ovh}}$): The preamble field of the received packet is used to compensate for the channel effects and equalize data (frequency correction, noise estimation, synchronization), also for beamforming (training field), and further parameter specification like the MCS within the header block. We calculate the overhead within the packet as

$$\begin{aligned} T_{\text{p\_ovh}} &= \frac{1}{f_s}(\text{Preamble field length + Training field length}), \\ &\approx 5.3\,\mu\text{s}. \end{aligned} \tag{36}$$

Data time interval (T_{data}): We compute this time interval with the total of samples for the data sequence as

$$\begin{aligned} T_{\text{data}} &= \text{Data Length}/f_s \\ &\approx 260\,\mu\text{s}, \end{aligned} \tag{37}$$

where we assume the largest packet possible (corresponding to around 262 kB) within this standard, and in favor of the least packet overhead.

C. Evaluating the Average PAoI

Using the IEEE 80211.ad transmission-reception scheme, we balance the impact of overhead (due to MU localization and IRS reconfiguration) and packet losses (due to MU mobility) through the following steps

Step 1. (Evaluate the radius for the illuminated area): We compute this radius to observe a zero BER as the criteria.[18] The BER is evaluated using Monte Carlo simulations of the transmission-reception scheme depicted in Fig. 9. We performed a total of 50×10^4 packet emissions per radius value, which correspond to more than 100 Mbit emissions. Fig. 11 illustrates the evaluation of the perceived SNR (mean and variance) and BER at the receiver side as a function of the radius.[19] Based on the results in Fig. 11, we select

[15]The corresponding field length is evaluated through the Matlab code accessible in https://github.com/tkn-tub/IRS_Rejuvenation

[16]During the localization phase, the IRS is configured differently than for data transmission as it renders a narrow beam instead of a wide beam (as explained in Section III-A). We omit details on the IRS reconfiguration for localization as this step is abstracted with the localization time variable; still, information on this method is provided in [29, Algorithm 1].

[17]During localization, we assume a single transmitted byte per packet to afford the lowest overhead possible.

[18]We choose this criteria as our formulation for the average PAoI in (33) implicitly assumes free-of-errors transmissions in the illuminated area. To consider cases allowing higher BER, a new formulation is needed to evaluate the PAoI to consider communication errors.

[19]We remark that the MU will be located in the IRS's near field and the SNR calculations follow the near field evaluation in [26].

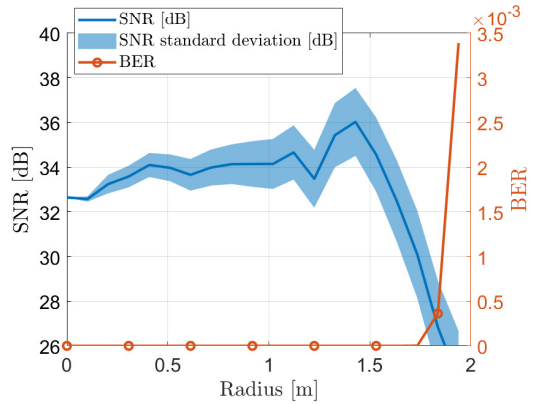

Fig. 11: Average SNR and BER as evaluated along the perimeter of the circle with radius given in the horizontal axis of this plot.

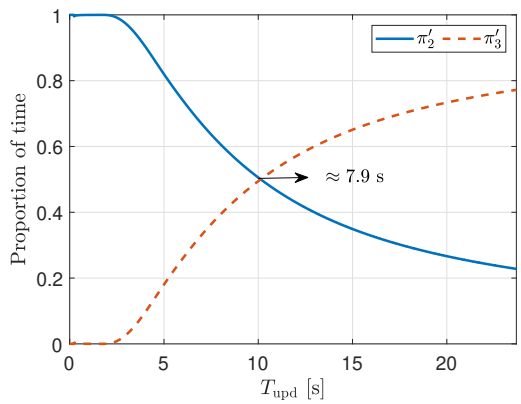

Fig. 12: Fraction of time in the inner and outer areas when $r_{\text{in}} = 1.7\,\text{m}$, $r_{\text{out}} = 3\,\text{m}$, $v = 1\,\text{m/s}$.

$r_{\text{in}} = 1.7\,\text{m}$ as the maximum radius to observe $\text{BER} = 0$ as per simulation.[20]

Step 2. (Evaluate the fraction of time the MU is inside and outside the illuminated area): For a given T_{upd}, we evaluate the fraction of time the MU is inside (π_2') and outside (π_3') the illuminated area using the formulation in (32). We remark that these fraction of times already include the overhead introduced by the MU localization and the IRS reconfiguration phase. We show the results of this evaluation in Fig. 12. As can be seen, if the IRS is updated more frequently than every $\approx 4.6\,\text{s}$, the MU spends more time in the illuminated area than outside it, and the average PAoI will be mostly evaluated as in (30).

At this point, we highlight that these two steps capture the influence of the IRS design on the communication link. For instance, a larger IRS effectively expands the illuminated area, thereby shifting to the right the intersection of the curves for π_2' and π_3' in Fig. 12. As a result, the overall system performance enhances due to the need to update the IRS less frequently.

Step 3. (Evaluate the average PAoI and select its minimum): We evaluate the average PAoI with (33) once the radius of the illuminated area is selected ($r_{\text{in}} = 1.7\,\text{m}$) and the fraction of time has been calculated, see Fig. 12. As a result, Fig. 13 depicts the average PAoI (for various radii) and the optimal update period T_{upd}.[21] With the plot in Fig. 13 the average PAoI ranges in the hundreds of microseconds, and the optimal update period results in the order of seconds.

Contextualizing these numbers, if we select the optimal update period in Fig. 13 when $r_{\text{in}} = 1.7\text{m}$, i.e., every $T_{\text{upd}} = 1.9\,\text{s}$ (see Fig. 8 for more details), the data transmissions between the AP and the MU are 6275 packets

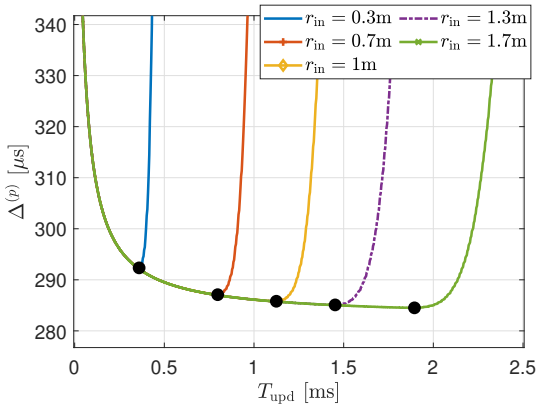

Fig. 13: Average PAoI with T_{upd} and various radius for the illuminated area.

in a run before reconfiguring the IRS again.[22] Reducing T_{upd} generates a larger overhead, and increasing it yields a larger BER. With this update time, the resulting overhead is around $\frac{T_{\text{ovh}}}{T_{\text{upd}}} \approx 9.6\,\%$ of the update period, after using Eq. (6) to evaluate T_{ovh}. This relatively small overhead is the minimum achievable one to balance the impact of the MU mobility.

Besides, visualizing the behavior for the average PAoI for smaller radii of the illuminated area provides some compelling insights. As depicted in Fig. 13, the optimal selection for T_{upd} shifts to the left with the decreasing radius as expected; however, the minimum average PAoI increases but not significantly. For reduced radii, the selection of the optimal T_{upd} becomes crucial, as the average PAoI increases dramatically for small deviations out of the optimal point; see, for instance, the case $r_{\text{in}} = 30\,\text{cm}$ in Fig. 13.[23]

D. Extending the Evaluation of the Average PAoI

Following the above steps, we can evaluate the optimal update periodicity for different mobility model configurations. Fig. 14 comparatively depicts the T_{upd} versus the radius of the

[20]The evaluation of the BER in Fig. 11 accounts for the selected high-throughput MCS parameter, i.e., 12.6 as in Table I. A less order for this parameters yields a larger radius to observe a zero BER.

[21]For the purpose of illustration only, we evaluate the minimum of the different curves in Fig. 13 by selecting the smallest sample in the time sampled range. We obtain the samples by evaluating (33) in the time range 0.5×10^{-4} to 2.5 s with sampling interval 50 µs. This is an approximate value, and a more accurate solution can be evaluated by derivative-free (e.g., bisection) or gradient-based (e.g., Newton's) methods.

[22]We do this calculation with the ratio $T_{\text{upd}}/(T_{\text{ppdu}} + \text{Idle Time})$, where the Idle time is 20 µs; see Table I.

[23]The case when $r_{\text{in}} = 30\,\text{cm}$ becomes relevant for secure wireless communications (see [47]) where smaller coverage areas are preferred and the selection of the IRS configuration time becomes more relevant.

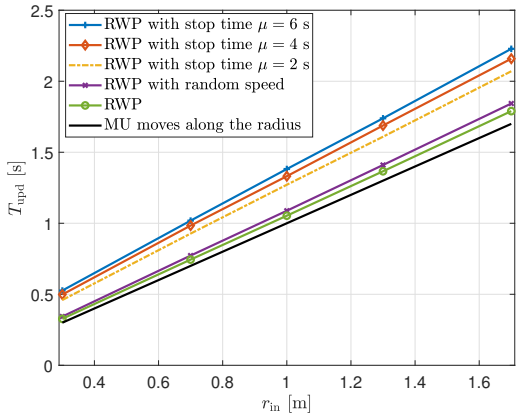

Fig. 14: Optimum value of T_{upd} versus the inner circle radius for various mobility models.

illuminated area and includes other mobility models such as RWP with stop time and with random speed. For comparisons, we also plot the case when the user moves straight from the center to the perimeter of the illuminated area along the radius. This represents the worst-case trajectory as the MU leaves the illuminated area in the least time. As for the stop time, we implemented a random variable following an exponential distribution for various average times; see [30, Section 3.6]. As for the random speed, we consider the MU changes the speed per waypoint randomly in the range 0.1 to $1.5\,\mathrm{m/s}$ and follows a uniform distribution; see [30, Section 3.5.1]. As Fig. 14 illustrates, the relation between the update period and the radius of the illuminated area is almost linear. In the RWP model, T_{upd} is slightly larger than the time interval the MU takes to travel from the center to the illuminated area's border, i.e., $T_{\mathrm{upd}} \approx \frac{r_{\mathrm{in}}}{v}$. However, this is not the case for RWP with stop time where T_{upd} results larger (in this case in the range 0.25 to $1\,\mathrm{s}$) than the traveling time from the center to the perimeter of the illuminated area.

VII. Conclusions

We presented a methodology to evaluate the optimal update period for the IRS elements in mobile scenarios using an average PAoI framework. This methodology allowed us to develop a reconfiguration design with low overhead. This solution plays a significant role in reducing the communication overhead while preserving the QoS of the link. Given the geometry and the size of the area illuminated by the IRS, where the QoS criteria are met, our approach evaluates the proportion of time the MU will be in the illuminated area to determine later the optimal IRS update period. This procedure minimizes the average PAoI and helps jointly balance the impact of overhead and MU mobility. We illustrated the applicability of these calculations considering the practical case of a WiFi link in the mmWave band. We find that the update period is in the ms range and is almost linearly increasing with the radius of the IRS illumination area. The resulting minimum information freshness is in the order of the hundreds of $\mu\mathrm{s}$.

This paper unlocks several new potential research directions. One direction is to extend the AoI framework to a multi-link scenario, that is, with multiple MUs and IRS. In the case of multiple MUs, the IRS need to be split among the MUs, impacting the achieved SNR and the size of the illuminated area. Another interesting research direction is the optimization of other system parameters, such as the number of IRS elements and the transmission policies. For instance, finding the optimal transmission policy for the MU is particularly relevant to avoid transmission while the MU is outside the illuminated area, allowing it to extend its battery lifetime. To this end, a Markov decision process (MDP) can be formulated to determine the optimal transmission policy that jointly maximizes the battery lifetime while minimizing the average PAoI. Moreover, IRS splitting could be considered for multiple MU scenarios. This would require finding the optimal policy for jointly updating multiple segments of the same IRS. Another relevant extension is the consideration of more complex channel models for evaluating the average PAoI metric. For instance, including multipath models or small-scale fading will impact the perceived SNR, thereby impacting the resulting average PAoI metric. Furthermore, an experimental evaluation of the considered system would allow the validation of the proposed theoretical framework. Measurement campaigns can be conducted to evaluate the main metrics and correlate their impact on information freshness.

VIII. Acknowledgments

We want to thank Dr. Anatolij Zubow from TU Berlin for the valuable comments on this manuscript. This work was supported in part by the Federal Ministry of Education and Research (BMBF, Germany) within the 6G Research and Innovation Cluster 6G-RIC under Grant 16KISK020K. Jamali's work was supported in part by the Deutsche Forschungsgemeinschaft (DFG, German Research Foundation) within the Collaborative Research Center MAKI (SFB 1053, Project-ID 210487104) and in part by the LOEWE initiative (Hesse, Germany) within the emergenCITY center [LOEWE/1/12/519/03/05.001(0016)/72].

References

[1] Q. Wu and R. Zhang, "Towards Smart and Reconfigurable Environment: Intelligent Reflecting Surface Aided Wireless Network," *IEEE Communications Magazine*, vol. 58, no. 1, pp. 106–112, Jan. 2020.

[2] Z. Chen, G. Chen, J. Tang, et al., "Reconfigurable-Intelligent-Surface-Assisted B5G/6G Wireless Communications: Challenges, Solution, and Future Opportunities," *IEEE Communications Magazine*, vol. 61, no. 1, pp. 16–22, Jan. 2023.

[3] M. Najafi, V. Jamali, R. Schober, and H. V. Poor, "Physics-Based Modeling and Scalable Optimization of Large Intelligent Reflecting Surfaces," *IEEE Transactions on Communications*, vol. 69, no. 4, pp. 2673–2691, Apr. 2021.

[4] W. Wang and Z. Wei, "Joint Beam Training and Positioning for Intelligent Reflecting Surfaces Assisted Millimeter Wave Communications," *IEEE Transactions on Wireless Communications*, vol. 20, no. 10, pp. 6282–6297, Oct. 2021.

[5] V. Jamali, M. Najafi, R. Schober, and H. V. Poor, "Power Efficiency, Overhead, and Complexity Tradeoff of IRS Codebook Design—Quadratic Phase-Shift Profile," *IEEE Communications Letters*, vol. 25, no. 6, pp. 2048–2052, Jun. 2021.

[6] C. Hu, L. Dai, S. Han, and X. Wang, "Two-Timescale Channel Estimation for Reconfigurable Intelligent Surface Aided Wireless Communications," *IEEE Transactions on Communications*, vol. 69, no. 11, pp. 7736–7747, Nov. 2021.

[7] F. Saggese, V. Croisfelt, R. Kotaba, C. Stylianopoulos, G. C. Alexandropoulos, and P. Popovski, "On the Impact of Control Signaling in RIS-Empowered Wireless Communications," *IEEE Open Journal of the Communications Society*, vol. 5, pp. 4383–4399, 2024.

[8] P. Cai, J. Zong, X. Luo, Y. Zhou, S. Chen, and H. Qian, "Downlink Channel Tracking for Intelligent Reflecting Surface-Aided FDD MIMO Systems," *IEEE Transactions on Vehicular Technology*, vol. 70, no. 4, pp. 3341–3353, Apr. 2021.

[9] F. Laue, M. Garkisch, V. Jamali, and R. Schober, "Performance Tradeoff of RIS Beam Training: Overhead vs. Achievable SNR," in *56th Asilomar Conference on Signals, Systems, and Computers*, Pacific Grove, CA, Oct. 2022.

[10] H. Hashida, Y. Kawamoto, and N. Kato, "Adaptive Pilot Interval Optimization for Intelligent Reflecting Surface-Aided Communication Systems," *IEEE Transactions on Vehicular Technology*, vol. 71, no. 7, pp. 7963–7966, Jul. 2022.

[11] N. Pappas, A. A.-E. Abd-Elmagid, B. Zhou, W. Saad, and H. S. Dhillon, *Age of Information: Foundations and Applications*. Cambridge, United Kingdom: Cambridge University Press, 2023, p. 479.

[12] W. Lyu, Y. Xiu, S. Yang, P. L. Yeoh, Y. Li, and Z. Zhang, "Weighted Sum Age of Information Minimization in Wireless Networks with Aerial IRS," *IEEE Transactions on Vehicular Technology*, pp. 1–5, 2022.

[13] M. Samir, M. Elhattab, C. Assi, S. Sharafeddine, and A. Ghrayeb, "Optimizing Age of Information Through Aerial Reconfigurable Intelligent Surfaces: A Deep Reinforcement Learning Approach," *IEEE Transactions on Vehicular Technology*, vol. 70, no. 4, pp. 3978–3983, Apr. 2021.

[14] X. Fan, M. Liu, Y. Chen, S. Sun, Z. Li, and X. Guo, "RIS-Assisted UAV for Fresh Data Collection in 3D Urban Environments: A Deep Reinforcement Learning Approach," *IEEE Transactions on Vehicular Technology*, vol. 72, no. 1, pp. 632–647, Jan. 2023.

[15] W. Lyu, Y. Xiu, J. Zhao, and Z. Zhang, "Optimizing the Age of Information in RIS-Aided SWIPT Networks," *IEEE Transactions on Vehicular Technology*, vol. 72, no. 2, pp. 2615–2619, Feb. 2023.

[16] X. Feng, S. Fu, F. Fang, and F. R. Yu, "Optimizing Age of Information in RIS-Assisted NOMA Networks: A Deep Reinforcement Learning Approach," *IEEE Wireless Communications Letters*, vol. 11, no. 10, pp. 2100–2104, Oct. 2022.

[17] C. Wang, Z. Li, T.-X. Zheng, D. W. K. Ng, and N. Al-Dhahir, "Intelligent Reflecting Surface-Aided Full-Duplex Covert Communications: Information Freshness Optimization," *IEEE Transactions on Wireless Communications*, vol. 22, no. 5, pp. 3246–3263, May 2023.

[18] Z. Shi, H. Wang, Y. Fu, X. Ye, G. Yang, and S. Ma, "Outage Performance and AoI Minimization of HARQ-IR-RIS Aided IoT Networks," *IEEE Transactions on Communications*, vol. 71, no. 3, pp. 1740–1754, Mar. 2023.

[19] W. Jiang, B. Ai, M. Li, W. Wu, and X. Shen, "Average Age-of-Information Minimization in Aerial IRS-Assisted Data Delivery," *IEEE Internet of Things Journal*, vol. 10, no. 17, pp. 15 133–15 146, Sep. 2023.

[20] C. Wang, Z. Li, Y. Zhao, D. W. K. Ng, and N. Al-Dhahir, "Age of Information Minimization in Intelligent Reflecting Surface-Aided Covert Communications," in *IEEE Global Communications Conference (GLOBECOM 2022), 7th IEEE Workshop on 5G and Beyond Wireless Security (WirelessSec 2022)*, Rio de Janeiro, Brazil: IEEE, Dec. 2022.

[21] M. Ali, M. Elhattab, M. A. Arfaoui, and C. Assi, "Optimizing Age of Information in RIS-Empowered Uplink Cooperative NOMA Networks," *IEEE Transactions on Network and Service Management*, pp. 897–907, 2023.

[22] K. Xie, G. Cai, G. Kaddoum, and J. He, "Performance Analysis and Resource Allocation of STAR-RIS-Aided Wireless-Powered NOMA System," *IEEE Transactions on Communications*, vol. 71, no. 10, pp. 5740–5755, Oct. 2023.

[23] G. Zhang, Y. Lu, Y. Lin, Z. Zhong, Z. Ding, and D. Niyato, "AoI Minimization in RIS-aided SWIPT Systems," *IEEE Transactions on Vehicular Technology*, pp. 1–6, 2023.

[24] Q. Sun, J. Niu, X. Zhou, T. Jin, and Y. Li, "AoI and Data Rate Optimization in Aerial IRS-Assisted IoT Networks," *IEEE Internet of Things Journal*, pp. 1–13, 2023.

[25] M. Segata, M. Lestas, P. Casari, et al., "Enabling Cooperative Autonomous Driving Through mmWave and Reconfigurable Intelligent Surfaces," in *18th IEEE/IFIP Conference on Wireless On demand Network Systems and Services (WONS 2023)*, Madonna di Campiglio, Italy: IEEE, Jan. 2023.

[26] G. C. Alexandropoulos, V. Jamali, R. Schober, and H. V. Poor, "Near-Field Hierarchical Beam Management for RIS-Enabled Millimeter Wave Multi-Antenna Systems," in *12th Sensor Array and Multichannel Signal Processing Workshop (SAM 2022)*, Trondheim, Norway: IEEE, Jun. 2022.

[27] V. Jamali, G. C. Alexandropoulos, R. Schober, and H. V. Poor, "Low-to-Zero-Overhead IRS Reconfiguration: Decoupling Illumination and Channel Estimation," *IEEE Communications Letters*, vol. 26, no. 4, pp. 932–936, Apr. 2022.

[28] F. Zafari, A. Gkelias, and K. K. Leung, "A Survey of Indoor Localization Systems and Technologies," *IEEE Communications Surveys & Tutorials*, vol. 21, no. 3, pp. 2568–2599, 2019.

[29] G. Zhang, D. Zhang, Y. He, J. Chen, F. Zhou, and Y. Chen, "Multi-Person Passive WiFi Indoor Localization With Intelligent Reflecting Surface," *IEEE Transactions on Wireless Communications*, vol. 22, no. 10, pp. 6534–6546, Oct. 2023.

[30] C. Bettstetter, H. Hartenstein, and X. Costa-Pérez, "Stochastic Properties of the Random Waypoint Mobility Model," *Wireless Networks*, vol. 10, no. 5, pp. 555–567, Sep. 2004.

[31] E. Cinlar, *Introduction to stochastic processes*. Englewood Cliffs, NJ: Prentice Hall, 1975, p. 395.

[32] R. A. Howard, *Dynamic probabilistic systems*. Wiley, 1971, vol. II, p. 1107.

[33] S. Garg, A. Puliafito, M. Telek, and K. S. Trivedi, "Analysis of software rejuvenation using Markov Regenerative Stochastic Petri Net," in *6th International Symposium on Software Reliability Engineering (ISSRE 1995)*, Toulouse, France: IEEE, Oct. 1995.

[34] H. Choi, V. G. Kulkarni, and K. S. Trivedi, "Markov regenerative stochastic Petri nets," *Performance Evaluation*, vol. 20, no. 1-3, pp. 337–357, May 1994.

[35] T. Murata, "Petri nets: Properties, analysis and applications," *Proceedings of the IEEE*, vol. 77, no. 4, pp. 541–580, Apr. 1989.

[36] J. L. Peterson, "Petri Nets," *ACM Computing Surveys*, vol. 9, no. 3, pp. 223–252, Sep. 1977.

[37] S. Redner, *A Guide to First-Passage Processes*. Cambridge University Press, 2001, p. 328.

[38] A. Papoulis, *Probability, Random Variables and Stochastic Processes*, 4th ed. Boston, MA: McGraw Hill, 2002, p. 852.

[39] A. Kosta, N. Pappas, and V. Angelakis, "Age of Information: A New Concept, Metric, and Tool," *Foundations and Trends in Networking*, vol. 12, no. 3, pp. 162–259, Nov. 2017.

[40] M. Costa, M. Codreanu, and A. Ephremides, "On the Age of Information in Status Update Systems With Packet Management," *IEEE Transactions on Information Theory*, vol. 62, no. 4, pp. 1897–1910, Apr. 2016.

[41] T. Nitsche, C. Cordeiro, A. B. Flores, E. W. Knightly, E. Perahia, and J. Widmer, "IEEE 802.11 ad: directional 60 GHz communication for multi-Gigabit-per-second Wi-Fi," *IEEE Communications Magazine*, vol. 52, no. 12, pp. 132–141, 2014.

[42] IEEE, "Wireless LAN Medium Access Control (MAC) and Physical Layer (PHY) Specifications," IEEE, Std 802.11-2020, Feb. 2021.

[43] WLAN PPDU Structure, https://ch.mathworks.com/help/wlan/gs/dmg-ppdu-structure.html.

[44] ETSI, "Reconfigurable Intelligent Surfaces (RIS); Communication Models, Channel Models, Channel Estimation and Evaluation Methodology," European Telecommunications Standards Institute, GR RIS 003 V1.1.1, Jun. 2023. [Online]. Available: https://www.etsi.org/deliver/etsi_gr/RIS/001_099/003/01.01.01_60/gr_RIS003v010101p.pdf.

[45] IRS-assisted link with 802.11ad, https://github.com/jorge-torresgomez/IRS_802_11ad.

[46] H. Kamoda, S. Iwasaki, J. Tsumochi, T. Kuki, and O. Hashimoto, "60-GHz Electronically Reconfigurable Large Reflectarray Using Single-Bit Phase Shifters," *IEEE Transactions on Antennas and Propagation*, vol. 59, no. 7, pp. 2524–2531, Jul. 2011.

[47] X. Yu, D. Xu, Y. Sun, D. W. K. Ng, and R. Schober, "Robust and Secure Wireless Communications via Intelligent Reflecting Surfaces," *IEEE Journal on Selected Areas in Communications*, vol. 38, no. 11, pp. 2637–2652, Nov. 2020.

Jorge Torres Gómez received the B.Sc., M.Sc., and Ph.D. degrees from the Technological University of Havana, CUJAE, Cuba, in 2008, 2010, and 2015, respectively. He is currently with the Telecommunication Networks Group, Department of Telecommunication Systems, Technical University of Berlin. He holds a position as head of educational activities at the IEEE Germany Section, supporting teaching activities and chairing conference events in education. His research interests include molecular communications, nanonetworks, the age of information, and digital signal processing.

Joana Angjo is with the Telecommunications Network Group group at the School of Electrical Engineering and Computer Science, TU Berlin. She received her B.Sc. degree in Electronics and Communication Engineering from Istanbul Technical University and her M.Sc. degree on Electrical and Electronics Engineering from Koç University in 2020 and 2022, respectively. During her M.Sc studies, she was part of the Communications Research and Innovation Laboratory and Nanonetworking Research Group. Her research interests include wireless communications, reconfigurable intelligent surfaces, and molecular communications.

Moritz Garkisch (Graduate Student Member, IEEE) received the B.Sc. degree in Electrical Engineering and the M.Sc. degree in Advanced Signal Processing and Communications Engineering from the Friedrich–Alexander-Universität Erlangen–Nürnberg, Germany, in 2020 and 2022, respectively, where he is currently pursuing the Ph.D. degree in Electrical Engineering at the Institute for Digital Communication. His main research interests are cellular communication, intelligent reflecting surfaces, sensing/localization, as well as wireless communication in general.

Vahid Jamali (Senior Member, IEEE) received the doctoral degree (with distinctions) from Friedrich-Alexander University Erlangen-Nürnberg (FAU) in 2019. He has been an Assistant Professor with the Technical University of Darmstadt (TUDa), since 2022, leading the Resilient Communication Systems Lab. Prior to joining TUDa, he held academic appointments at Princeton University (2021–2022) and FAU (2019– 2021), as a Post-Doctoral Researcher; and at Stanford University as a Visiting Researcher in 2017. His research interests include wireless and molecular communications. He has served as an Associate Editor of the IEEE TRANSACTIONS ON COMMUNICATIONS and IEEE COMMUNICATIONS LETTERS, an Editor-at-Large at IEEE OPEN JOURNAL OF THE COMMUNICATIONS SOCIETY as well as a Vice-Chair for the IEEE ComSoc – German chapter. He has received several awards for his publications including the Best Paper Awards from the IEEE ICC in 2016, the ACM NanoCom in 2019, the Asilomar CSSC in 2020, and the IEEE WCNC in 2021; and the Best Journal Paper Award (Literaturpreis) from the German Information Technology Society (ITG) in 2020.

Robert Schober (S'98–M'01–SM'08–F'10) was born in Neuendettelsau, Germany, in 1971. He received the Diplom (Univ.) and Ph.D. degrees in electrical engineering from the Friedrich-Alexander-Universität Erlangen–Nürnberg in 1997 and 2000, respectively. From 2001 to 2002, he was a Post-Doctoral Fellow with the University of Toronto, Canada, sponsored by the German Academic Exchange Service. Since 2002, he has been with The University of British Columbia, Vancouver, Canada, where he is currently a Full Professor. Since 2012, he has been an Alexander von Humboldt Professor and the Chair of Digital Communication with the Friedrich-Alexander-Universität Erlange–Nürnberg, Germany. His research interests include the broad areas of communication theory, wireless communications, and statistical signal processing. Dr. Schober is a fellow of the Canadian Academy of Engineering and the Engineering Institute of Canada. From 2012 to 2015, he served as an Editor-in-Chief of the IEEE TRANSACTIONS ON COMMUNICATIONS. Since 2014, he has been the Chair of the Steering Committee of the IEEE TRANSACTIONS ON MOLECULAR, BIOLOGICAL, AND MULTISCALE COMMUNICATIONS. Furthermore, he is a Member-at-Large of the Board of Governors of the IEEE Communications Society. He has received several awards for his work, including the 2002 Heinz MaierLeibnitz Award of the German Science Foundation, the 2004 Innovations Award of the Vodafone Foundation for Research in Mobile Communications, the 2006 UBC Killam Research Prize, the 2007 Wilhelm Friedrich Bessel Research Award of the Alexander von Humboldt Foundation, the 2008 Charles McDowell Award for Excellence in Research from UBC, a 2011 Alexander von Humboldt Professorship, and a 2012 NSERC E.W.R. Steacie Fellowship. In addition, he has received several best paper awards for his research.

Falko Dressler is full professor and Chair for Telecommunication Networks at the School of Electrical Engineering and Computer Science, TU Berlin. He received his M.Sc. and Ph.D. degrees from the Dept. of Computer Science, University of Erlangen in 1998 and 2003, respectively. Dr. Dressler has been associate editor-in-chief for IEEE Trans. on Network Science and Engineering, IEEE Trans. on Mobile Computing and Elsevier Computer Communications as well as an editor for journals such as IEEE/ACM Trans. on Networking, Elsevier Ad Hoc Networks, and Elsevier Nano Communication Networks. He has been chairing conferences such as IEEE INFOCOM, ACM MobiSys, ACM MobiHoc, IEEE VNC, IEEE GLOBECOM. He authored the textbooks Self-Organization in Sensor and Actor Networks published by Wiley & Sons and Vehicular Networking published by Cambridge University Press. He has been an IEEE Distinguished Lecturer as well as an ACM Distinguished Speaker. Dr. Dressler is an IEEE Fellow, an ACM Fellow, and an AAIA Fellow. He is a member of the German National Academy of Science and Engineering (acatech). He has been serving on the IEEE COMSOC Conference Council and the ACM SIGMOBILE Executive Committee. His research objectives include next generation wireless communication systems in combination with distributed machine learning and edge computing for improved resiliency. Application domains include the internet of things, cyber-physical systems, and the internet of bio-nano-things.